



Optimization of process parameters for gas-powder flow behavior in the coaxial nozzle during laser direct metal deposition based on numerical simulation

Kai Zhao¹ · Kun Yang¹ · Mingzhi Chen¹ · Zhandong Wang² · Erke Wu¹ · Guifang Sun¹ 

Received: 15 September 2023 / Accepted: 1 January 2024 / Published online: 10 January 2024
© The Author(s), under exclusive licence to Springer-Verlag London Ltd., part of Springer Nature 2024

Abstract

Laser direct metal deposition (DMD) can supply a new method in the fields of surface modification and near-net forming. The powder flow behavior and its convergence characteristics play a crucial role in the deposition quality during the DMD process. In this research, the k - ε turbulence model based on the computational fluid dynamics (CFD) modeling method was innovatively employed to establish the numerical model of the gas-powder flow. Then, the dense discrete phase model (DDPM) was utilized in this gas-powder coupling model to accurately calculate the collision between particles as well as between particles and inner wall of the nozzle. Afterward, the response surface method (RSM) was carried out to design the numerical simulation scheme, analyze a series of simulation results, explore the correlation between the process parameters and the responses, and establish the prediction model of powder convergence characteristics. Furthermore, the process parameters were optimized by considering the influence of defocusing amount, with smaller powder spot diameter and higher maximum powder mass concentration as optimization objectives. It was found that the prediction model of powder convergence characteristics demonstrated a high degree of accuracy and reliability. The single-deposition track exhibited better deposition quality fabricated with the optimized process parameters. The research method and results mentioned in the present study were expected to provide significant theoretical guidance for the selection and application of process parameters during the laser direct metal deposition process.

Keywords Laser direct metal deposition · Coaxial nozzle · Numerical simulation · Prediction model · Process parameter optimization

1 Introduction

Laser direct metal deposition (DMD) is an advanced surface modification technique with promising applications in aerospace, offshore equipment, and energy transportation [1–4]. During the DMD process, a laser beam is utilized to irradiate the substrate, resulting in the formation of a molten pool. Consequently, the powder material is introduced into the molten pool via transport by the carrier gas, wherein it undergoes the processes of melting and solidification to ultimately yield the deposited material. The interaction between

gases (powder carrier gas and shielding gas) and powder, as well as the interaction among powders, significantly impacts the quality of the deposited material [5–7]. The disclosure of these interactions is essential for the regulation of deposition quality and the optimization of deposition efficiency.

The conventional approaches, such as employing high-speed cameras for direct observation, fail to provide a comprehensive characterization of the aforementioned interactions. Furthermore, the powder flow behavior and the interaction between gas and powder within the deposition head cannot be effectively captured through a high-speed camera. An alternative approach to address this issue is through numerical modeling, which offers a cost-effective means to comprehend these intricate interactions. An accurate model plays an important role in process prediction and analysis system control. A series of related studies have been carried out based on numerical modeling. Guo et al. [8] studied the influence of powder carrier gas flow rate on powder convergences, and

✉ Guifang Sun
gfsun@seu.edu.cn

¹ School of Mechanical Engineering, Southeast University, Nanjing 211189, Jiangsu, China

² College of Mechanical and Electronic Engineering, Nanjing Forestry University, Nanjing 210037, China

the results showed a negative correlation between the mass concentration of the powder and the flow rate of the powder carrier gas. Liu et al. [9] determined the powder mass concentration distribution at different locations and analyzed the influence of powder jet velocity and particle size on the powder mass concentration distribution using the weight measurement method. The results demonstrated a high level of concordance between the simulation outcomes and the measured data. Stankevich et al. [10] utilized the Reynolds-averaged Navier-Stokes (RANS) equation to solve the transport characteristics of powder and investigate the impact of process parameters on gas flow behavior on particle motion trajectories. Based on the Euler-Lagrange method, the gas-powder coupling model of a four-way nozzle was established by Gao et al. [11]. Furthermore, it also supplemented with relevant experimental verification to elucidate the impact of particle properties and other parameters on powder flow behavior.

Currently, the research on powder flow behavior and its convergence characteristics primarily focuses on single-factor analysis, with limited exploration of the multi-factor coupling effect. Meanwhile, the powder transport process is extremely complex, encompassing collisions between particles as well as between particle and the inner wall of the nozzle. These collision behaviors will remarkably change the angle of convergence and velocity distribution of the powder streaming [12]. However, the aforementioned collision behaviors were often overlooked in most of the previous studies, thereby resulting in significant discrepancies in simulation outcomes during the powder transportation.

In the current research, a coaxial four-way nozzle is taken as the research object. A numerical gas-powder coupling model is proposed, which incorporates previously overlooked factors (collisions between particles as well as between particles and the inner wall of the nozzle), to elucidate the interactions between powder, gas flows (powder carrier gas and shielding gas), and the nozzle. Ultimately, it reveals the convergence characteristics of the powder flow. The RSM is used to design the numerical simulation scheme and analyze a series of simulated results. Based on a comprehensive multiple-factor analysis, the prediction model of powder convergence characteristics is established and validated. The process parameters are optimized by considering the influence of defocusing amount, with smaller powder spot diameter and higher powder mass concentration as optimization objectives. Within the optimized process parameters, superior deposition quality is observed in single-deposition tracks.

2 Modeling of the gas-powder flow

The gas-powder flow is a typical multiphase flow, characterized by the continuous phase of gas and the discrete phase of powder [13]. The dense discrete phase model (DDPM)

enables the precise analysis of the multiphase flow, especially its inherent coupling effect. Compared with the discrete phase mode (DPM) and discrete element method (DEM), DDPM incorporates particle collision and voidage, while simplifying the collision processing to effectively reduce memory usage and data processing without compromising calculation accuracy [14]. In the current research, the Euler-Lagrange model is used, and a comprehensive description of this model can be found elsewhere [15–17].

2.1 Model adjustment

The model is established based on the following assumptions [12, 18]:

- (1) the effect of laser on powder convergence is not considered;
- (2) the powder carrier gas and the shielding gas are viscous and incompressible;
- (3) substrate and powder materials are homogenous and solid;
- (4) the motion of powder is primarily influenced by the drag force exerted by the gas flow, the inelastic collisions between powders, and the interactions with the inner wall of the nozzle.

2.2 Continuous phase modeling

The continuous phase flow behavior requires the solution of a set of Navier-Stokes equations [19]. Considering the turbulent nature of gas-powder flow, the Reynolds-averaged Navier-Stokes (RANS) equation is employed to solve for the temporal average of both velocity and pressure fields [18, 20]. Particularly, the evaluation of turbulent viscosity in the equation requires the use of turbulence models. The most commonly used turbulence model is the standard k - ϵ turbulence model, which is a typical two-equation model that requires solving for turbulent kinetic energy (k) and turbulent kinetic energy dissipation rate (ϵ) [13, 21, 22]. The time-mean governing equations of turbulence are shown below [23].

Mass conservation equation:

$$\frac{\partial}{\partial x_i} (\rho u_i) = 0 \quad (1)$$

where ρ is the gas density, and u_i and x_i represent the velocity and position, respectively.

Momentum conservation equation:

$$\frac{\partial}{\partial x_j} (\rho u_i u_j) = -\frac{\partial p}{\partial x_i} + \frac{\partial \tau_{ij}}{\partial x_j} + \rho g_i \quad (2)$$

where g is the acceleration of gravity and τ_{ij} is the viscous force tense calculated by Eq. (3):

$$\tau_{ij} = \left[(\mu + \mu_t) \left(\frac{\partial \mu_i}{\partial x_i} + \frac{\partial \mu_j}{\partial x_j} \right) \right] - \frac{2}{3} \mu_t \frac{\partial \mu_i}{\partial x_i} \delta_{ij} \quad (3)$$

where μ is the molar viscosity, and for $i = j$, $\delta_{ij} = 1$, otherwise $\delta_{ij} = 0$. μ_t is the turbulent viscosity which is expressed by Eq. (4):

$$\mu_t = \rho C_\mu \frac{k^2}{\varepsilon} \quad (4)$$

The standard k - ε turbulence model is adopted [24].

Conservation of kinetic energy of turbulence k :

$$\frac{\partial}{\partial x_j} (\rho \mu_i k) = \frac{\partial}{\partial x_j} \left(\frac{\mu_t}{\sigma_k} \frac{\partial k}{\partial x_j} \right) + G_k + G_b - \rho \varepsilon \quad (5)$$

Conservation of dissipation of kinetic energy of turbulence ε :

$$\frac{\partial}{\partial x_j} (\rho \mu_j \varepsilon) = \frac{\partial}{\partial x_j} \left(\frac{\mu_t}{\sigma_\varepsilon} \frac{\partial \varepsilon}{\partial x_j} \right) + C_1 \frac{\varepsilon}{k} (G_k + G_b) - C_2 \rho \frac{\varepsilon^2}{k} \quad (6)$$

$$G_k = \mu_t \left(\frac{\partial \mu_i}{\partial x_j} + \frac{\partial \mu_j}{\partial x_i} \right) \frac{\partial \mu_i}{\partial x_j} \quad (7)$$

$$G_b = -g_i \frac{\mu_t}{\rho Pr_t} \frac{\partial \rho}{\partial x_i} \quad (8)$$

$$Pr_t = \frac{\mu_t C_p}{k_t} \quad (9)$$

where G_k represents the generation of turbulence kinetic energy due to the velocity gradient, G_b is the turbulent kinetic energy caused by buoyancy, and Pr_t is the turbulent Prandtl number. The empirical constants $C_\mu = 0.9$, $C_1 = 1.44$, $C_2 = 1.92$, $\sigma_k = 1.0$, and $\sigma_\varepsilon = 1.3$ in all of the aforementioned equations are determined through iterative processes to account for arbitrary turbulence.

2.3 Discrete phase modeling

The equation of discrete phase (powder material) motion in Lagrange coordinates can be expressed by Eq. (10):

$$m_p \frac{du_p}{dt} = m_p \frac{(u - u_p)}{\tau_r} + m_p \frac{g(\rho_p - \rho)}{\rho_p} + F \quad (10)$$

where m_p is the particle mass, u_p is the particle velocity, ρ_p is the density of the particle, u is the continuous phase velocity, ρ is the continuous phase density, F is the additional force, and τ_r is the relaxation time which can be calculated by Eq. (11) [16, 25]:

$$\tau_r = \frac{\rho_p d_p^2}{18\mu C_D Re} \quad (11)$$

where μ is the molar viscosity of the continuous phase, d_p is the diameter of the particle, and Re is the relative Reynolds number which is evaluated by Eq. (12):

$$Re = \rho d_p \frac{|u_p - u|}{\mu} \quad (12)$$

According to the Haider-Levenspiel model [11, 26], the drag force coefficient of non-spherical particles C_D can be expressed by Eq. (13):

$$C_D = \frac{24}{Re} (1 + A \cdot Re^B) + \frac{C}{1 + \frac{D}{Re}} \quad (13)$$

where the coefficients A , B , C , and D can be calculated by Eqs. (14)–(17):

$$A = \exp(2.3288 - 6.4581\varphi + 2.4489\varphi^2) \quad (14)$$

$$B = \exp(0.0964 + 0.5565\varphi) \quad (15)$$

$$C = \exp(4.905 - 13.8944\varphi + 18.4222\varphi^2 - 10.2599\varphi^3) \quad (16)$$

$$D = \exp(1.4681 + 12.2584\varphi - 20.7322\varphi^2 + 15.8855\varphi^3) \quad (17)$$

where φ is the sphericity coefficient of the particle which is evaluated by Eq. (18):

$$\varphi = \frac{s_p}{S_p} \quad (18)$$

where S_p is the actual surface area of the particle, s_p is the surface area when the particle shape is completely spherical at the same volume, and $0 < \varphi < 1$.

2.4 Initial and boundary conditions

The physical diagram and the corresponding 3D solid model of the Precilec coaxial four-way nozzle are shown in Fig. 1(a, b). The calculation domain can be obtained by establishing the model of the cavity region inside the nozzle and the air region below the nozzle within a certain range, in accordance with the inverse working principle of the DMD process shown in Fig. 1(c). The corresponding calculation domain and boundary conditions are shown in Fig. 1(d). The initial conditions are set as follows: pressure $p(0) = 10^5$ Pa, temperature $T(0) = 300$ K, and velocity $u(0) = 0$ m/s at time $t = 0$ s. On the channel walls, the boundary conditions of the particles are $V'_{pn} = -k_n V_{pn}$, $V'_{p\tau} = V_{p\tau}$. The collisions between the particle and the inner wall of

Fig. 1 **a** The physical diagram of the Precilec nozzle, **b** the 3D solid model of the nozzle, **c** the working principle of the DMD process, and **d** the computational domain partitioning and boundary condition setting

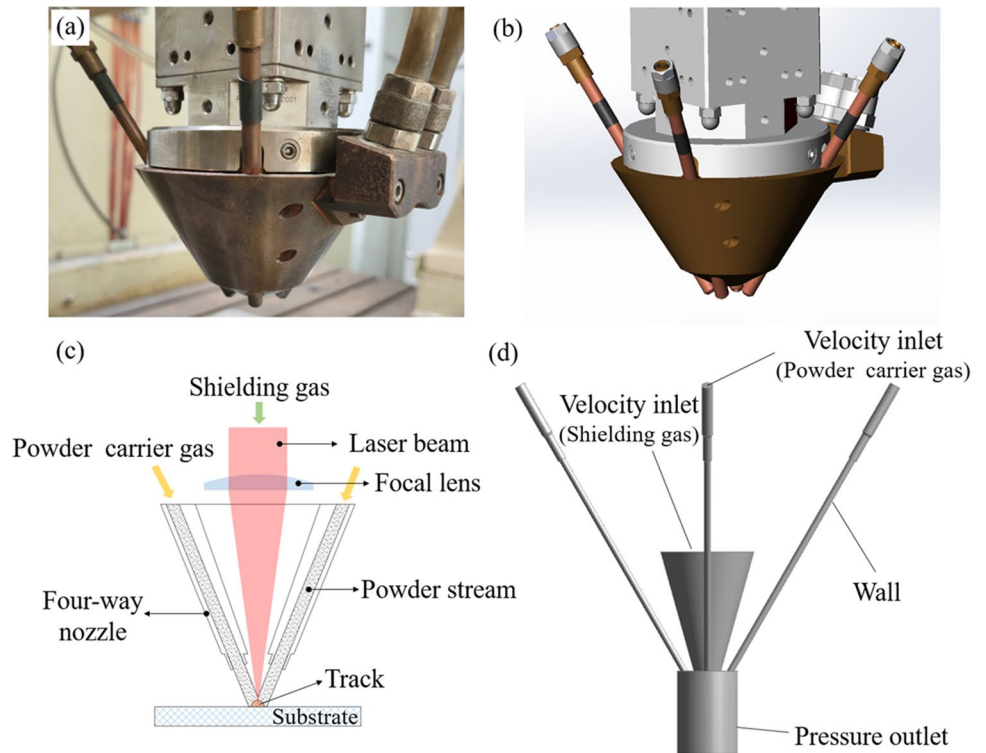


Table 1 Physical properties of argon

Relative molecular mass	Density (kg/m ³)	Viscosity (kg/m ⁻⁵)
39.95	1.62	2.13 × 10 ⁻⁵

the nozzle as well as among particles are characterized by inelasticity [27]. When the collision occurs, the tangential velocity of the particle remains constant, the normal velocity has a certain degree of attenuation, k_n is the normal velocity recovery coefficient, and $0 < k_n < 1$. In the current research, the value of k_n is set to 0.9 [24, 28].

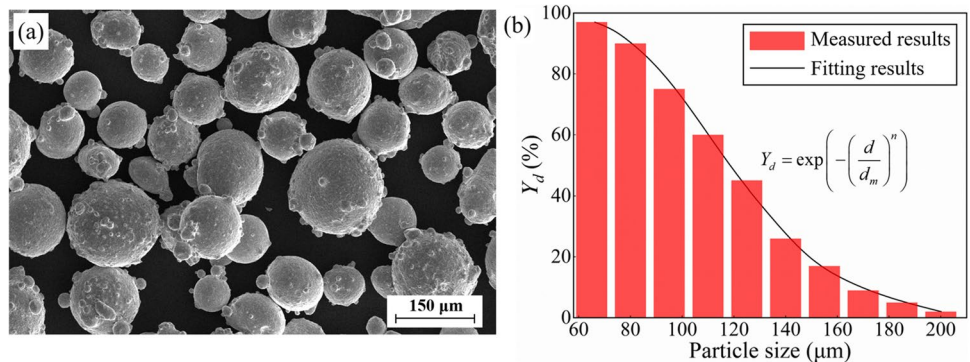
3 Experimental details

3.1 Material

The process parameters associated with the powder feeding process consist of the powder carrier gas flow rate and the powder feeding rate. The powder carrier gas and shielding gas are chosen to be high-purity argon (Ar). The physical properties of Ar are shown in Table 1.

The powder material used in the current research is 316L stainless steel ($\rho = 7980 \text{ kg/m}^3$), which is prepared by gas atomization. The morphology of the 316L powder is depicted in Fig. 2(a). The size distribution of powders can be accurately characterized by the Rosin-Rammler model.

Fig. 2 **a** 316L powder morphology and **b** comparison of measured and fitting results of the particle size



On this basis, the mass fraction of particles with a diameter greater than d (Y_d) is mathematically represented by Eq. (19) [17]:

$$Y_d = \exp\left(-\left(\frac{d}{d_m}\right)^n\right) \tag{19}$$

where d_m is the mean size of the particle and n is the size spread parameter. The particles can be categorized into distinct size ranges, each with varying mass fractions as indicated in Table 2.

The particle size distribution measurement results presented in Table 2 are fitted using Eq. (19), as depicted in Fig. 2(b). It is evident that the fitting results exhibit excellent agreement with the measured data. The curve fitting analysis of the data presented in Table 2 enables the determination of the average particle size, d_m . This corresponds to the d value at $Y_d = e^{-1}$, and it can be found that d_m is equal to 130 μm . In addition, the size spread parameter n can be evaluated by Eq. (20):

$$n = \frac{\ln(-\ln Y_d)}{\ln(d/d_m)} \tag{20}$$

By substituting the measurement results of particle size distribution in Table 2 for Y_d and d/d_m into Eq. (20) and calculating the average value, then the size spread parameter n of 4.0 is obtained. All size distribution parameters are summarized in Table 3.

3.2 High-speed camera

The powder flow behavior monitoring in this research is conducted using a high-speed camera (Memrecan HX-7S; NAC, Japanese). The AFS VR105mm f/2.8G IF-ED prime lens is used to shoot the powder streaming. The high-speed camera

Table 2 Mass fraction in particle diameter range

Diameter, d (μm)	Mass fraction with diameter greater than d , Y_d (%)
65	97
80	90
95	75
110	60
125	45
140	26
155	17
170	9
185	3
200	2

Table 3 Summary of particle size distribution parameters

Mean diameter (μm)	130
Maximum diameter (μm)	200
Minimum diameter (μm)	65
Number of diameters (#)	10
Spread parameter	4.0

and infrared guide light are positioned on opposite sides of the powder streaming, as depicted in Fig. 3, to observe the trajectories of powder streaming. Afterward, the results are analyzed to determine the powder convergence distribution and its velocity.

The laser system (Trudisk 3006; Trumpf, Germany) is employed to conduct the corresponding experiments with the output laser power of $P = 1500$ W, laser diameter of $D = 3$ mm, and scanning speed of $V = 600$ mm/min, which can be utilized for validating the benefits of process parameter optimization methods (Section 4.4).

4 Results and discussion

4.1 Gas-powder coupling model

The plane with the maximum powder mass concentration (C_{max}) is selected as the cross-section where the powder spot is located. Subsequently, the distance (H) between the powder spot and the bottom of the nozzle is determined, as illustrated in Fig. 4(a). The calculation boundary for determining the powder spot diameter is set at 14% of its peak concentration [29], as shown in Fig. 4(b). Consequently, the powder spot diameter (D) can be obtained.

To obtain the actual values of D and H from the experimental observation (Fig. 3(b)), we take the actual width of the nozzle bottom exit edge ($B_1 = 10$ mm) as a reference. On this basis, these values can be converted using Eqs. (21) and (22).

$$H = B_1 \frac{H_0}{B_0} \tag{21}$$

$$D = B_1 \frac{D_0}{B_0} \tag{22}$$

Due to the inherent difficulty in accurately measuring the maximum powder mass concentration [27], in this research, the average mass concentration (C_{avg3}) of the powder spot ($D = 3$ mm) is selected for quantitative comparison between the simulation and the experiment. The weight measurement method is employed to determine the powder mass concentration [16], as shown in Fig. 5. The approximation of C_{avg3} can be calculated using Eq. (23):

Fig. 3 **a** Illustration of the experimental observation and **b** the powder streaming captured by the high-speed camera

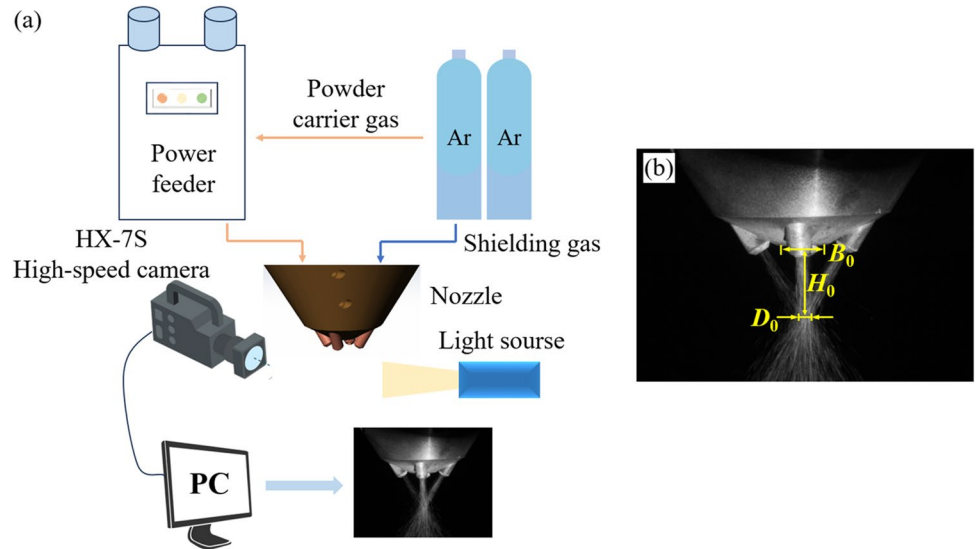


Fig. 4 **a** Powder mass concentration distribution in vertical section, and **b** the definition of powder spot diameter

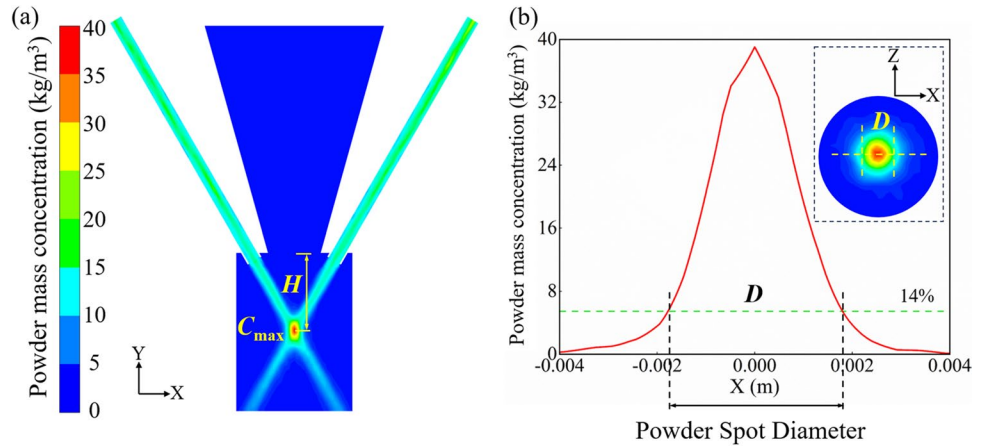
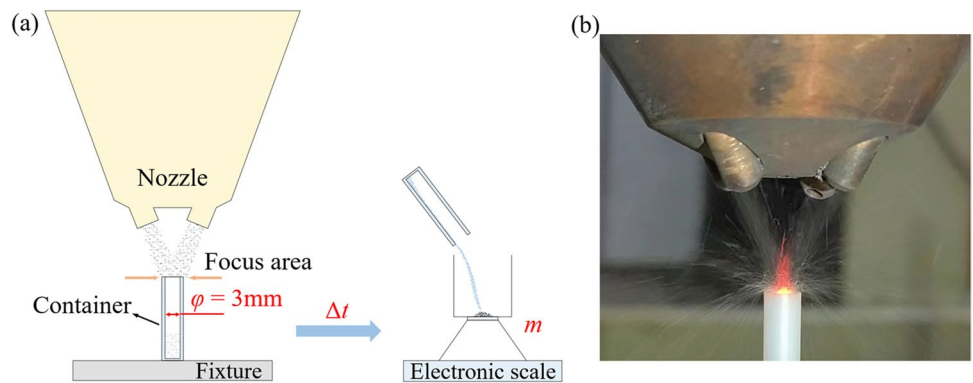


Fig. 5 Weight measurement method used to determine the powder mass concentration. **a** Schematic diagram and **b** experimental diagram



$$C_{avg3} = \frac{m}{\frac{\pi \cdot \varphi^2}{4} \cdot v \cdot \Delta t} \quad (23)$$

where Δt represents the duration for powder collection, φ is the internal diameter of the tube, m is the mass of the powder obtained within a specific collection duration, and v is the

velocity of the powder. The velocity (v) can be determined by meticulously tracking the trajectory of an individual powder frame by frame captured using a high-speed camera.

The trajectory length of the powder within 20 frames is determined by capturing the position of a single particle in the initial and 21st frame using a high-speed camera

Fig. 6 The position of a single powder under different frames. **a** Frame 1 and **b** frame 21

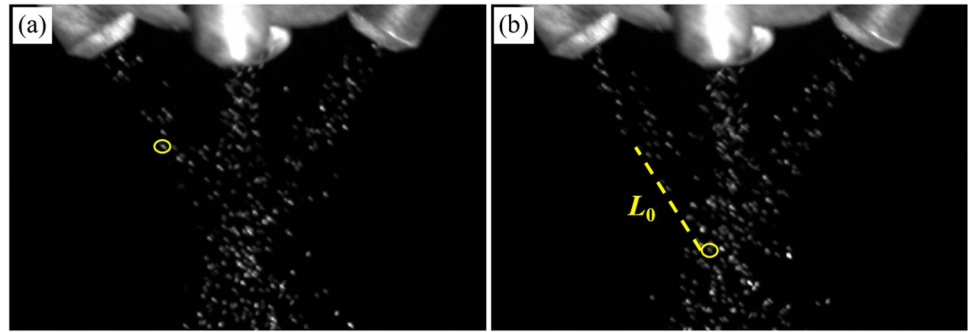


Table 4 Process parameters for model validation

Group	CG (L/min)	SG (L/min)	PF (r/min)
1	2	6	1.0
2	5	12	2.5
3	8	12	3.5
4	11	24	1.5

operating at a rate of 20,000 frame/s, as illustrated in Fig. 6. Consequently, the mathematical expression of the powder velocity is illustrated in Eq. (24).

$$v = \frac{B_1 \cdot L_0 \cdot 20000}{B_0 \cdot 20} \tag{24}$$

The reliability of the simulation model is validated through experimental measurements, encompassing four

distinct sets of parameters including powder carrier gas flow rate (*CG*), shielding gas flow rate (*SG*), and powder feeding rate (*PF*), as presented in Table 4. The values of C_{avg3} , *D*, and *H* obtained by simulations and experiments are presented in Figs. 7 and 8. The errors between the simulation and experiment results are within 12% (Fig. 8(d)), indicating that the proposed model in the current research demonstrates exceptional computational accuracy and reliability, thereby providing significant guidance for selecting process parameters in the DMD process.

4.2 Influence of process parameters on gas-powder flow behavior

In this research, the response surface method is employed to design the simulation scheme, to investigate the impact of powder carrier gas flow rate, shielding gas flow rate, and powder feeding rate, as well as their coupling effects on the powder flow behavior and its convergence characteristics.

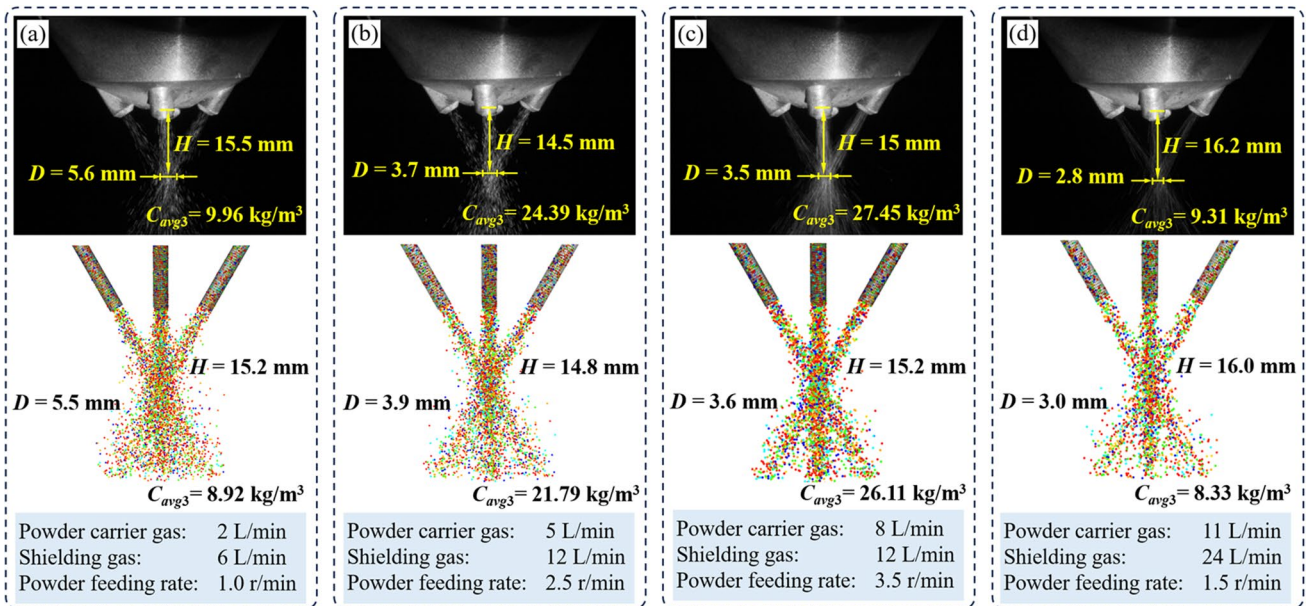
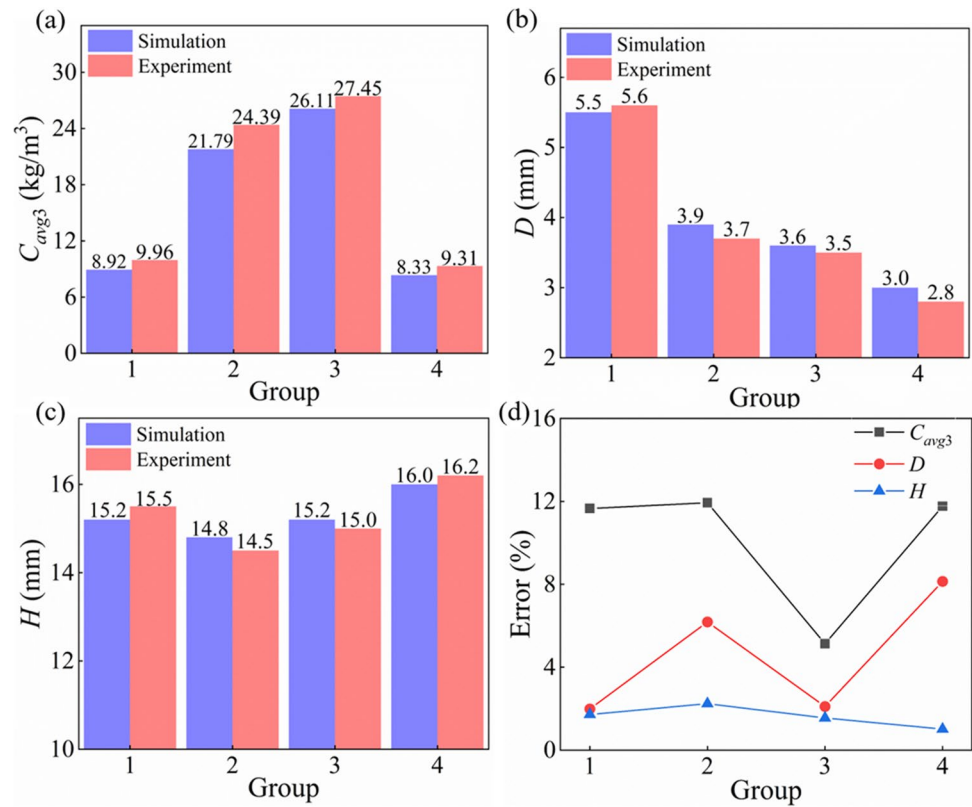


Fig. 7 Simulation and experiment results of powder flow. **a** Group 1, **b** group 2, **c** group 3, and **d** group 4

Fig. 8 Comparison of simulation and experiment results. **a** C_{avg3} , **b** D , **c** H , and **d** error



The level of process parameters is shown in Table 5. The input parameters encompass powder carrier gas flow rate, shielding gas flow rate, and powder feeding rate. Correspondingly, the responses include maximum powder mass concentration, powder spot diameter, and the distance between the powder spot and the bottom of the nozzle. The design scheme along with its corresponding simulated values is presented in Table 6.

The trend observed in Fig. 9(a) demonstrates a reduction in the maximum powder mass concentration with the increase in powder carrier gas flow rate; however, a decrease in the maximum powder mass concentration is observed when the gas flow rate is set at 2 L/min, as illustrated in Fig. 9(a). During powder transportation, the velocity of the powder is always lower than powder carrier gas [18]. The disparity between their velocities will be more pronounced with an increase in the powder carrier gas flow rate. Consequently, this disparity leads to an intensified drag force exerted by the powder carrier gas on the powder, thereby

leading to an increase in the velocity of the powder (Eqs. (10)–(17)). An increase in powder velocity will result in a reduction of powder mass concentration, according to Eq. (24). However, the powder mass concentration distribution trend exhibits an inverse relationship when the powder carrier gas flow rate is lower. This phenomenon can be attributed to a diminished impact of the powder carrier gas on particles at a lower flow rate [29]. The interaction between the particle and the inner wall of the nozzle, as well as inter-particle collisions, plays a crucial role in powder transportation. This results in an augmented normal velocity component of the particle at the nozzle exit, resulting in an increased divergence angle of the powder jet and subsequently reducing the powder mass concentration.

The powder spot diameter exhibits an obvious negative correlation with the powder carrier gas flow rate, as depicted in Fig. 9(b). As detailed above, the enhancement of the powder carrier gas flow rate will lead to an increased drag effect exerted by the gas on the powder. The powder is hindered in

Table 5 Level of process parameters

Process parameters	Unit	Level				
		– 2	– 1	0	1	2
CG	L/min	2	5	8	11	14
SG	L/min	0	6	12	18	24
PF	r/min	0.5	1	1.5	2.5	3.5

Table 6 Design scheme and the corresponding simulated values

Case	CG (L/min)	SG (L/min)	PF (r/min)	C_{max} (kg/m ³)	D (mm)	H (mm)
1	2	0	0.5	10.01	4.38	14.85
2	2	6	1.0	12.30	5.49	15.24
3	2	12	1.5	16.36	5.76	15.63
4	2	18	2.5	23.61	5.68	15.86
5	2	24	3.5	27.74	6.33	16.02
6	5	0	1.0	15.45	3.61	15.24
7	5	6	1.5	21.65	3.78	15.22
8	5	12	2.5	33.11	3.94	14.83
9	5	18	3.5	43.11	4.19	14.83
10	5	24	0.5	7.14	3.70	16.02
11	8	0	1.5	17.85	3.42	15.24
12	8	6	2.5	29.39	3.47	14.83
13	8	12	3.5	39.03	3.58	15.24
14	8	18	0.5	6.14	3.34	15.63
15	8	24	1.0	10.58	3.91	16.02
16	11	0	2.5	20.47	3.62	14.83
17	11	6	3.5	35.26	3.20	14.41
18	11	12	0.5	8.61	2.29	16.43
19	11	18	1.0	15.65	2.28	16.53
20	11	24	1.5	15.91	3.05	16.04
21	14	0	3.5	22.75	3.67	14.83
22	14	6	0.5	6.76	2.22	16.82
23	14	12	1.0	12.68	2.34	16.43
24	14	18	1.5	15.20	2.57	16.04
25	14	24	2.5	16.62	3.45	15.63

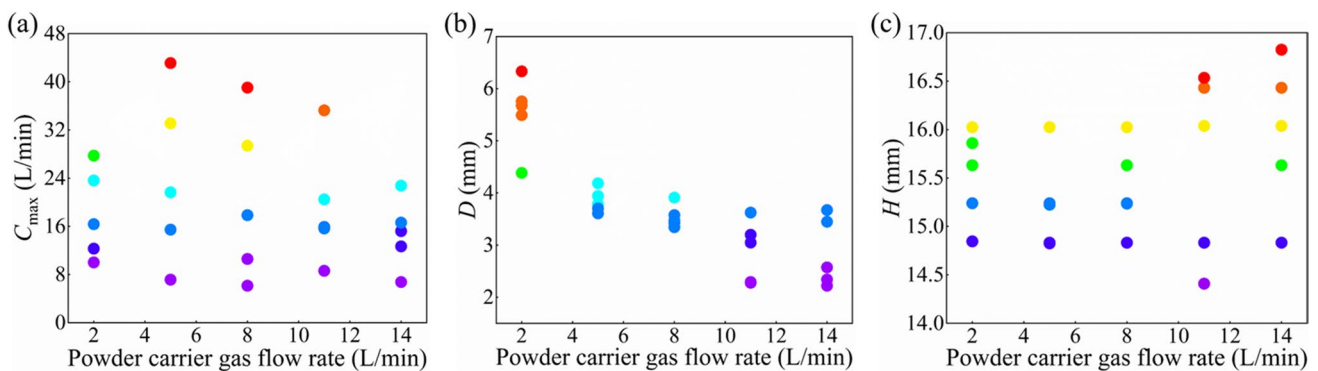


Fig. 9 Effect of powder carrier gas flow rate on response. **a** C_{max} , **b** D , and **c** H

the normal direction of the inner wall of the nozzle, which brings out the increase of the particle tangential velocity component at the exit of the nozzle. The aforementioned phenomenon will lead to enhanced powder convergence and a reduction in powder spot diameter.

The distance between the powder spot and the bottom of the nozzle exhibits a positive correlation with the powder carrier gas flow rate on the whole, as illustrated in Fig. 9(c). The standard $k-\epsilon$ turbulence model is only applicable to the

core turbulent region (typically located far away from the wall), and cannot be directly applied to the near-wall region which experiences significant viscosity effects. In the current research, the non-equilibrium wall function based on the two-layer theory is employed to handle the near-wall flow, as shown in Fig. 10. It is assumed that the boundary layer near the wall consists of a viscous sublayer and a complete turbulent region. The velocity of the gas and powder in the viscous sublayer is lower compared to those in the

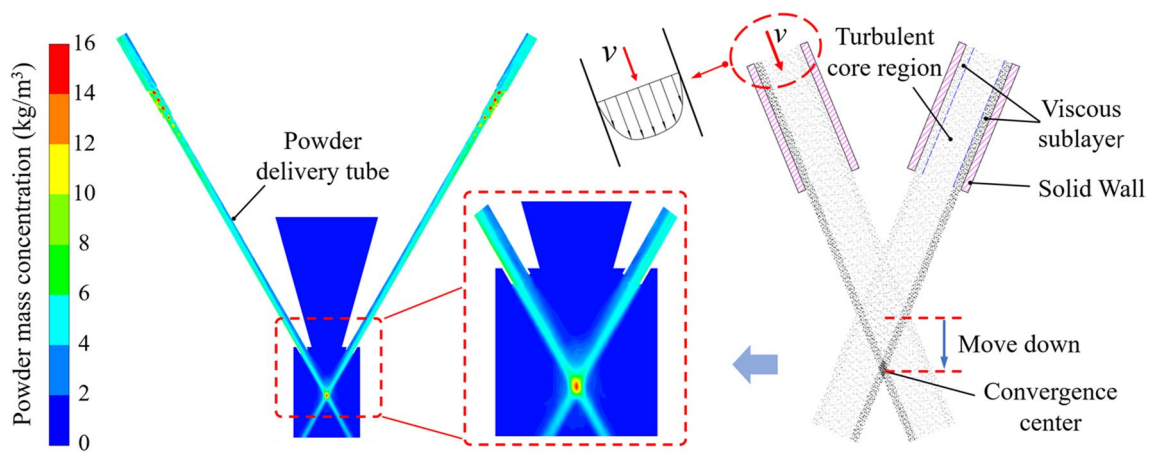


Fig. 10 Non-equilibrium wall function model and its simulation results

turbulent core region. The variations in flow rates across different regions of the powder delivery tube can be ascribed to the boundary layer effect. The boundary layer effect will become more pronounced as the powder carrier gas flow rate increases. In accordance with Eq. (24), the reduction in powder velocity will lead to an increase in the powder mass concentration. Thus, the powder mass concentration near the boundary layer will be higher than that in the turbulent core region. Meanwhile, considering the influence of gravity, a higher concentration of powder mass is observed in close proximity to the lower side of the powder delivery tube. As a comparison, the boundary layer effect is attenuated when the powder carrier gas flow rate is reduced, resulting in a more uniform distribution of powder mass concentration within the powder delivery tube (Fig. 4(a)). Consequently, an increased amount of powder carrier gas flow rate could lead to an elongation of the distance between the powder spot and the bottom of the nozzle (Fig. 9(c)).

The distance between the powder spot and the bottom of the nozzle will experience a noticeable increase due to the elevated flow rate of shielding gas, while there is no

significant impact on maximum powder mass concentration and powder spot diameter resulting from variations in the flow rate of shielding gas, as illustrated in Fig. 11. Due to the separate structure of the coaxial four-way nozzle, the powder carrier gas is discontinuous at the outlet, allowing for shielding gas flow through the gap. Therefore, the impact of shielding gas flow rate on maximum powder mass concentration and powder spot diameter is minimal. Based on this, the flow rate of the shielding gas can be appropriately increased during the DMD process to enhance the effectiveness of protection and obtain better deposition quality.

The augmentation of maximum powder mass concentration is prominently observed with the increase in powder feeding rate, as depicted in Fig. 12(a). Simultaneously, the probability and frequency of collision (particle-particle) will significantly increase with the rise of powder mass concentration. Therefore, the scattering angle of the powder jet at the nozzle exit expands, resulting in an expansion of the powder spot diameter (Fig. 12(b)). Meanwhile, it should be noted that the elevation of the powder feeding rate will weaken the influence of powder carrier gas and shielding

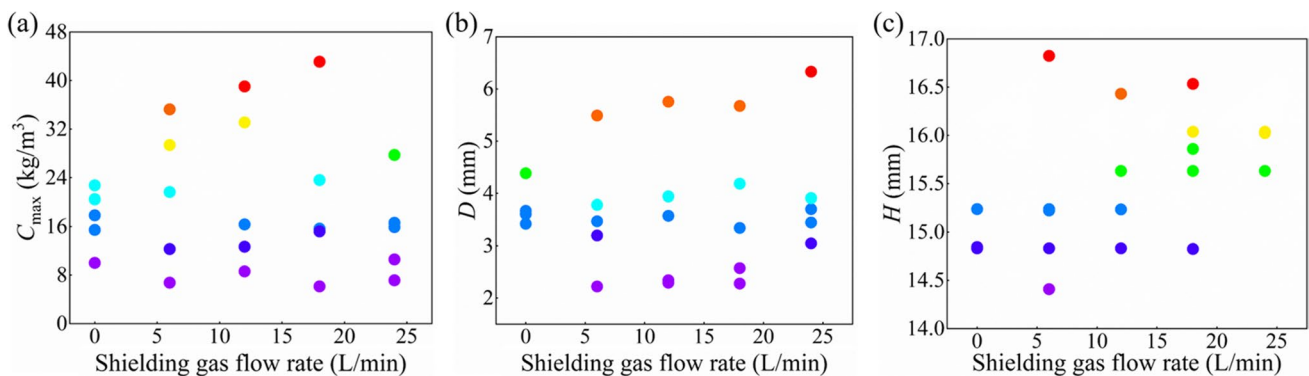


Fig. 11 Effect of shielding gas flow rate on response. **a** C_{max} , **b** D , and **c** H

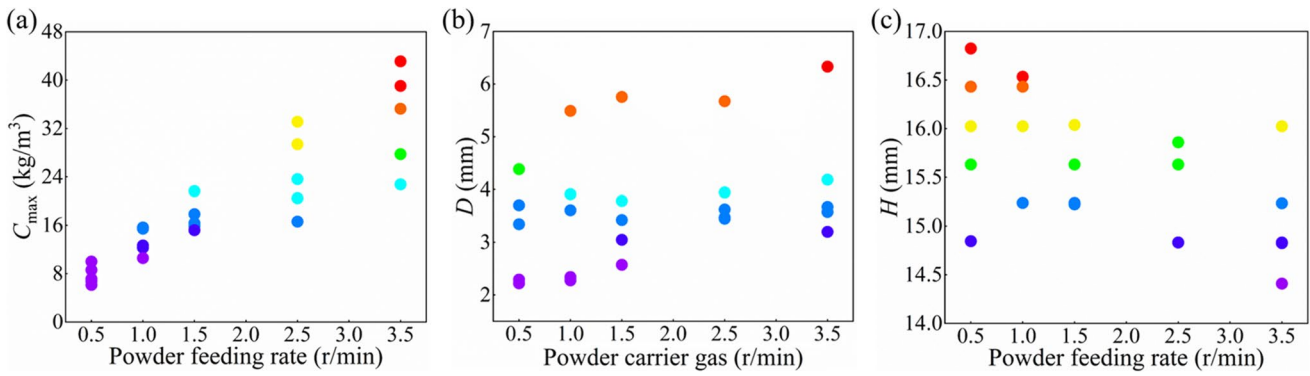


Fig. 12 Effect of powder feeding rate on response. **a** C_{max} , **b** D , and **c** H

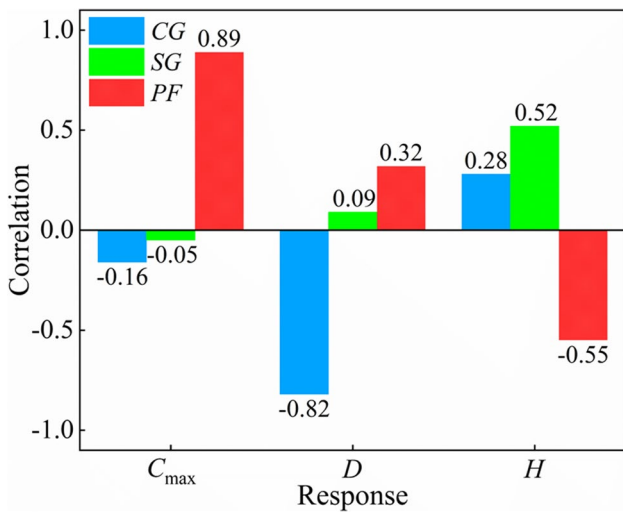


Fig. 13 Correlation analysis between process parameters and responses

gas flow rate on the powder spot location, as demonstrated in Fig. 12(c).

It is worth noting that the powder flow behavior and its convergence characteristics are not only influenced by a single factor but also affected by the coupling of multiple factors. The correlation between the responses (C_{max} , D , H) and process parameters is illustrated in Fig. 13. The powder mass concentration and powder spot diameter are primarily affected by the powder carrier gas flow rate and the powder feeding rate, while the value of H is mainly influenced by the shielding gas flow rate and the powder feeding rate. The 3D response surface is constructed to investigate the influence of coupling factors on the response as shown in Fig. 14. The maximum powder mass concentration initially increases and then decreases with the increase of the powder carrier gas flow rate when maintaining a constant powder feeding rate, as depicted in Fig. 14(a). Additionally, an increase in the powder feeding rate leads to a corresponding increase in the powder spot diameter when maintaining a constant powder carrier gas flow rate, as shown in Fig. 14(b). Moreover, for a low shielding gas flow rate, the value of H initially increases and then decreases with an increasing powder feeding rate;

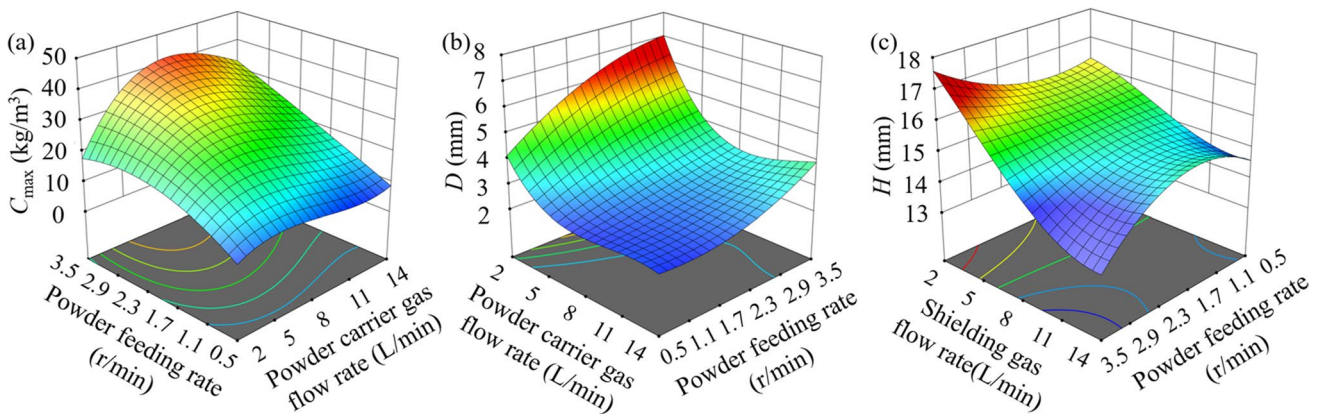


Fig. 14 3D response surface diagram. **a** C_{max} , **b** D , and **c** H

however, for a relatively high shielding gas flow rate, there is a positive correlation between the location of the powder spot and an increased powder feeding rate as depicted in Fig. 14 (c). The coupling of multiple factors exerts a substantial influence on the flow behavior of powder and its convergence characteristics during the DMD process. Therefore, it is imperative to adjust process parameters in accordance with specific requirements to attain optimal deposition formation.

4.3 Prediction model establishment

In the current research, the ternary quadratic orthogonal regression equation is employed to accurately establish the functional relationship between the process parameters and responses. Its general form is illustrated in Eq. (25):

$$\hat{y} = a + \sum_{j=1}^m b_j x_j + \sum_{k < j} b_{kj} x_k x_j + \sum_{j=1}^m b_{jj} x_j^2 \quad k = 1, 2, 3 \dots, m - 1 \tag{25}$$

where $\{a\}$, $\{b_j\}$, $\{b_{ij}\}$, and $\{b_{jj}\}$ are regression coefficients. The equations for the calculations of C_{max} , D , and H are shown below:

$$C_{max} = 0.545047 + 0.482748 \times CG - 0.519713 \times SG + 17.64068 \times PF + 0.146639 \times CG \times SG - 1.16499 \times CG \times PF - 0.431471 \times SG \times PF - 0.056987 \times CG^2 - 0.008309 \times SG^2 + 1.79963 \times PF^2 \tag{26}$$

$$D = 5.35243 - 0.448065 \times CG + 0.074712 \times SG + 0.049999 \times PF - 0.012929 \times CG \times SG + 0.095895 \times CG \times PF + 0.035224 \times SG \times PF + 0.015745 \times CG^2 - 0.000080 \times SG^2 - 0.272203 \times PF^2 \tag{27}$$

$$H = 14.94127 + 0.043141 \times CG + 0.060470 \times SG - 0.083365 \times PF - 0.004912 \times CG \times SG - 0.037745 \times CG \times PF + 0.008321 \times SG \times PF + 0.008375 \times CG^2 - 0.000211 \times SG^2 - 0.027127 \times PF^2 \tag{28}$$

As depicted in Fig. 15, a closer alignment of the scatter plot with the solid line indicates a smaller discrepancy between the simulation and fitting results. The majority of the original data points either fall on the fitting line or are evenly distributed on both sides, demonstrating high prediction accuracy for the proposed prediction model.

The reliability of the prediction model is further validated by randomly selecting four groups of process parameters that differed from those in Table 6, as presented in Table 7. Simulation and fitting results obtained from Eqs. (26)–(28) are conducted separately (Fig. 16(a–c)); the discrepancies between the fitting and simulation results are found to be below 9% (Fig. 16(d)), which can be considered an acceptable outcome for this prediction model.

4.4 Process parameter optimization

The morphology of the deposition layer is primarily influenced by the powder mass concentration and powder spot diameter. Increasing the maximum powder mass concentration appropriately and reducing the powder spot

Table 7 Process parameters for prediction model validation

Group	CG (L/min)	SG (L/min)	PF (r/min)
1	4	16	1.8
2	13	14	0.9
3	7	22	3
4	14	18	2

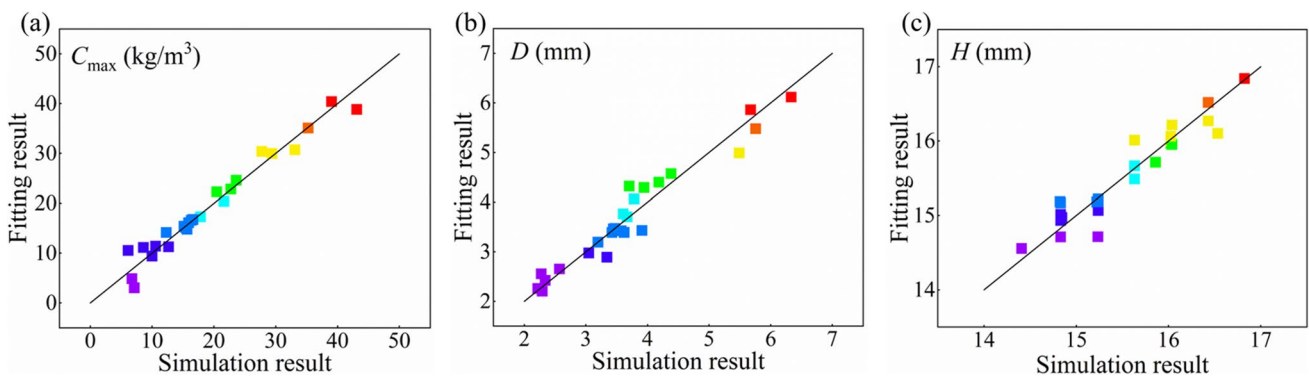
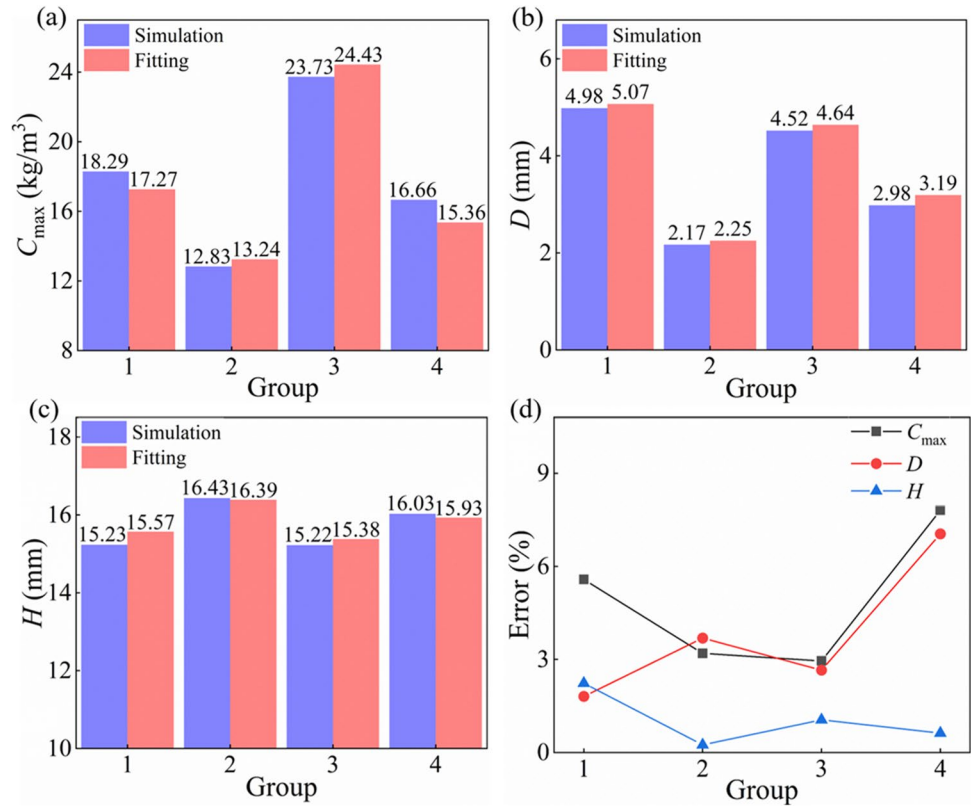


Fig. 15 Comparison of fitting and simulation results: **a** C_{max} , **b** D , and **c** H

Fig. 16 Results of prediction model validation. **a** C_{max} , **b** D , **c** H , and **d** error



diameter can effectively maximize the area of the deposition layer and enhance powder utilization efficiency. In light of the defocusing of the laser beam, precise control over the distance between the powder spot and the bottom of the nozzle is crucial for optimizing laser utilization. The current research conducts a comprehensive multi-objective optimization for maximum powder mass concentration, powder spot diameter, and the distance between the powder spot and the bottom of the nozzle by fully considering the effects of powder carrier gas flow rate, shielding gas flow rate, as well as powder feeding rate. The optimization objectives and conditions are presented in Table 8. The target region obtained based on the optimized conditions is illustrated in Fig. 17, and the corresponding optimization result is displayed in Table 9.

The advantages of the optimization results are validated through the single-deposition track experiment, for which 12 sets of process parameter combinations have been selected. The deposition layer can be divided into four sections based on its geometric characteristics, namely, the deposition layer itself, the molten pool, the heat-affected zones, and the substrate, as depicted in Fig. 18, where w represents the width of the deposition layer, h is the height of deposition layer, and h' signifies the molten depth.

The macroscopic morphology of the deposition layer is a crucial indicator for evaluating the quality of deposition. It necessitates not only achieving a certain depth of

Table 8 Optimization objectives and constraints

Name	Goal	Lower limit	Upper limit
CG (L/min)	In range	8	14
SG (L/min)	In range	0	24
PF (r/min)	In range	0.5	3.5
C_{max} (kg/m³)	In range	15	25
D (mm)	In range	2	3
H (mm)	In range	15	16

the molten pool to ensure proper metallurgical bonding but also incorporating a specific processing allowance to facilitate subsequent processing. The partially molten substrate diffuses into the melted powder, resulting in a dilution effect on the molten pool [30]. In the current research, the dilution rate η is employed to quantify the substrate diffusion outcome, which directly influences the metallurgical bonding characteristics of the deposition layer. The bonding properties are enhanced with a lower dilution rate within a specific range and the dilution rate η can be mathematically expressed by Eq. (29).

$$\eta = \frac{h'}{h + h'} \tag{29}$$

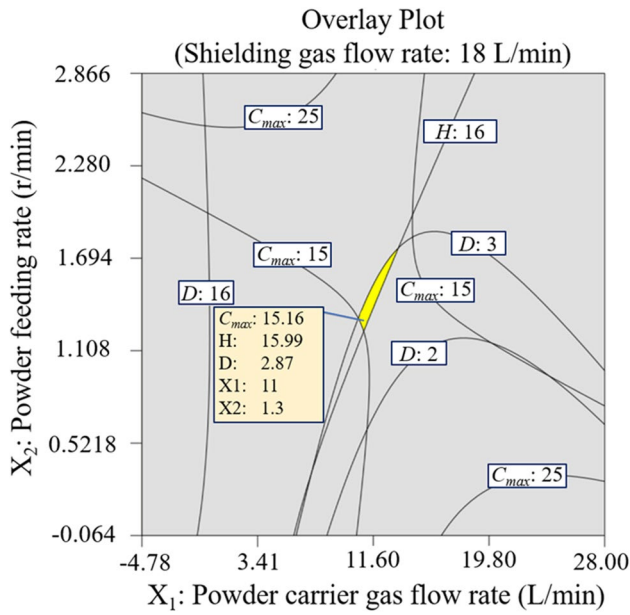


Fig. 17 Optimize target and regional distribution

Table 9 Optimization result

CG (L/min)	SG (L/min)	PF (r/min)	C_{max} (kg/m ³)	D (mm)	H (mm)
11	18	1.3	15.16	15.99	2.87

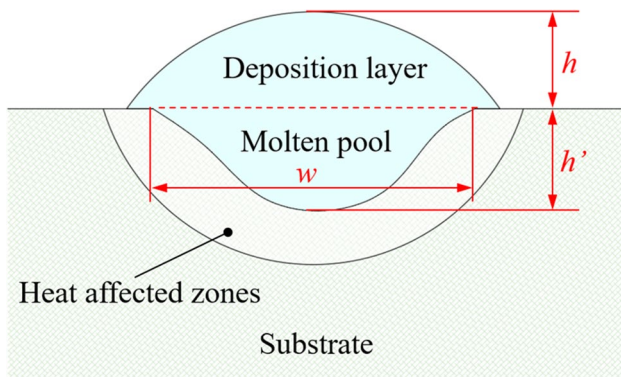


Fig. 18 Geometrical characteristics of deposition layer cross-section

The comprehensive quality of the deposition layer is assessed based on the analysis of the aspect ratio Φ , as expressed in Eq. (30). Within a specific range, higher values of the aspect ratio indicate better forming quality. The benchmark for evaluating the forming quality is typically set at $\Phi > 2$.

$$\Phi = \frac{w}{h} \tag{30}$$

The comparison of single-deposition track morphologies under different process parameters is illustrated in Fig. 19. When the aspect ratio becomes very small, the compactness between the deposition layer and the substrate will be compromised, leading to easy detachment, as shown in Fig. 19(d, e, f, g, l). Conversely, a high aspect ratio will result in an elevated probability of collapse occurring between deposition layers [31], as depicted in Fig. 19(b, c, i, g). The utilization of optimized process parameters, in comparison with alternative ones, can lead to a single deposition track with an appropriate aspect ratio for desired forming effects, as well as a notable dilution rate that ensures favorable bonding properties, as illustrated in Fig. 19 (a). Within the range of optimized process parameters, the single-deposition track demonstrates superior deposition quality. Therefore, the application of these optimized process parameters can yield significant advantages during the DMD process.

5 Conclusion

In the current research, a novel gas-powder coupling model that incorporates collisions between particles and between particle and inner wall of the nozzle was proposed to investigate powder flow behavior in laser direct metal deposition with coaxial nozzles. The influences of process parameters and their coupling effect on gas-powder flow behavior, the prediction model for powder convergence characteristics, and the determination of the optimal combination of process parameters were investigated. The findings were summarized as follows:

- (1) With the increase in powder carrier gas flow rate, both the maximum powder mass concentration and powder spot diameter decreased, while the distance between the powder spot and the bottom of the nozzle increased. Conversely, with the increase in the powder feeding rate, both the maximum powder mass concentration and powder spot diameter increased, while the distance between the powder spot and the bottom of the nozzle decreased.
- (2) The maximum powder mass concentration and powder spot diameter varied a little with shielding gas flow rates. However, the distance between the powder spot and the bottom of the nozzle exhibited a noticeable increase with the increase of shielding gas flow rate.
- (3) The distribution of powder mass concentration and powder spot diameter was primarily influenced by the powder carrier gas flow rate and the powder feeding rate. Meanwhile, the distance between the powder spot and the bottom of the nozzle was mainly affected by the shielding gas flow rate and the powder feeding rate.

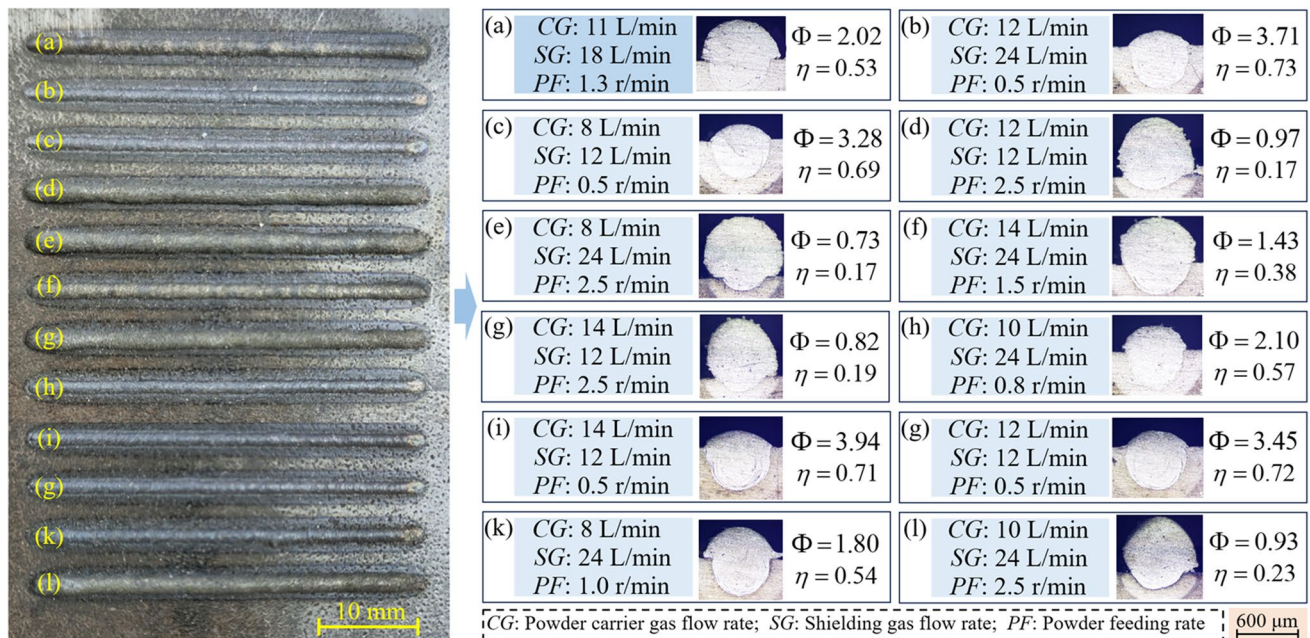


Fig. 19 Comparison of single deposition track morphology under various process parameters

- (4) The optimized process parameters for the powder carrier gas flow rate, shielding gas flow rate, and powder feeding rate were 11 L/min, 18 L/min, and 1.3 r/min, respectively. A superior deposition quality of a single track was fabricated with the optimized process parameters.

Author contribution Kai Zhao: methodology, investigation, and writing—original draft. Kun Yang: writing—review and editing. Mingzhi Chen: investigation. Zhandong Wang: investigation. Erke Wu: investigation. Guifang Sun: supervision, writing—review and editing, and funding acquisition.

Funding This work was supported by the fund for the Technical Field of the Basic Strengthening Plan of Science and Technology of a Certain Commission of China (grant numbers 2022-JCJQ-JJ-0117 and 2021-JCJQ-JJ-0088).

Declarations

Competing interests The authors declare no competing interests.

References

- Wang L, Lu BH (2022) Development of additive manufacturing technology and industry in China. *Chin J Eng Sci* 24:20
- Syed WUH, Pinkerton AJ, Li L (2006) Combining wire and coaxial powder feeding in laser direct metal deposition for rapid prototyping. *Appl Surf Sci* 252:4803–4808
- Liu Z, Jiang Q, Li T, Yan S, Zhang H, Xu B (2016) Environmental benefits of remanufacturing: a case study of cylinder heads remanufactured through laser cladding. *J Clean Prod* 133:1027–1103
- Onuikwe B, Heer B, Bandyopadhyay A (2018) Additive manufacturing of Inconel 718—Copper alloy bimetallic structure using laser engineered net shaping (LENS™). *Addit Manuf* 21:133–140
- Wang L, Wang S, Zhang Y, Yan W (2023) Multi-phase flow simulation of powder streaming in laser-based directed energy deposition. *Int J Heat Mass Transf* 212:124240
- Zhang J, Yang L, Zhang W, Qiu J, Xiao H, Liu Y (2020) Numerical simulation and experimental study for aerodynamic characteristics and powder transport behavior of novel nozzle. *Opt Lasers Eng* 126:105873
- Smith PH, Murray JW, Jones DO, Segal J, Clare AT (2021) Magnetically assisted directed energy deposition. *J Mater Process Technol* 288:116892
- Guo SR, Yin QQ, Cui LJ, Zheng B, Cao YL, Zeng WH (2020) Simulation and experimental research based on carrier gas flow rate on the influence of four-channel coaxial nozzle flow field. *Meas Control* 53:1571–1578
- Liu Z, Zhang HC, Peng S, Kim H, Du D, Cong W (2019) Analytical modeling and experimental validation of powder stream distribution during direct energy deposition. *Addit Manuf* 30:100848
- Stankevich S, Larionov N, Valdaytseva E (2021) Numerical analysis of particle trajectories in a gas–powder jet during the laser-based directed energy deposition process. *Metals* 11:2002
- Gao J, Wu C, Liang X, Hao Y, Zhao K (2020) Numerical simulation and experimental investigation of the influence of process parameters on gas-powder flow in laser metal deposition. *Opt Laser Technol* 125:106009
- Chai Q, He X, Xing Y, Sun GF (2023) Numerical study on the collision effect of particles in the gas-powder flow by coaxial nozzles for laser cladding. *Opt Laser Technol* 163:109449

13. Kovalev OB, Kovaleva IO, Smurov IY (2017) Numerical investigation of gas-disperse jet flows created by coaxial nozzles during the laser direct material deposition. *J Mater Process Technol* 249:118–127
14. Mirzaei M, Jensen PA, Nakhaei M, Wu H, Zakrzewski S, Zhou H, Lin W (2023) CFD-DDPM coupled with an agglomeration model for simulation of highly loaded large-scale cyclones: sensitivity analysis of sub-models and model parameters. *Powder Technol* 413:118036
15. Murer M, Furlan V, Formica G, Morganti S, Previtali B, Auricchio F (2021) Numerical simulation of particles flow in laser metal deposition technology comparing Eulerian-Eulerian and Lagrangian-Eulerian approaches. *J Manuf Process* 68:186–197
16. Taberner I, Lamikiz A, Ukar E, López De Lacalle LN, Angulo C, Urbikain G (2010) Numerical simulation and experimental validation of powder flux distribution in coaxial laser cladding. *J Mater Process Technol* 210:2125–2134
17. Wen SY, Shin YC, Murthy JY, Sojka PE (2009) Modeling of coaxial powder flow for the laser direct deposition process. *Int J Heat Mass Transf* 52:5867–5877
18. Doubenskaia M, Kulish A, Sova A, Petrovskiy P, Smurov I (2021) Experimental and numerical study of gas-powder flux in coaxial laser cladding nozzles of Precitec. *Surf Coat Technol* 406:126672
19. Lyu P, Jin L, Yan B, Zhu L, Yao J, Jiang K (2022) Numerical simulation and experimental investigation of the effect of three-layer annular coaxial shroud on gas-powder flow in laser cladding. *J Manuf Process* 84:457–468
20. Ibarra-Medina J, Pinkerton AJ (2010) A CFD model of the laser, coaxial powder stream and substrate interaction in laser cladding. *Phys Procedia* 5:337–346
21. Kovaleva I, Kovalev O, Zaitsev A, Smurov I (2013) Numerical simulation and comparison of powder jet profiles for different types of coaxial nozzles in direct material deposition. *Phys Procedia* 5:870–872
22. Liu Q, Li W, Yang K, Gao Y, Wang L, Chu X (2023) Analytical investigation into the powder distribution and laser beam-powder flow interaction in laser direct energy deposition with a continuous coaxial nozzle. *Adv Powder Technol* 34:104058
23. Serag-Eldin MA, Spalding DB (1979) Computations of three-dimensional gas-turbine combustion chamber flows. *J Eng Gas Turbine Power* 101:326–336
24. Bian Y, He X, Yu G, Li S, Tian C, Li Z, Zhang Y, Liu J (2022) Powder-flow behavior and process mechanism in laser directed energy deposition based on determined restitution coefficient from inverse modeling. *Powder Technol* 402:117355
25. Tan H, Zhang F, Wen R, Chen J, Huang W (2012) Experiment study of powder flow feed behavior of laser solid forming. *Opt Lasers Eng* 50:391–339
26. Haider A, Levenspiel O (1989) Drag coefficient and terminal velocity of spherical and nonspherical particles. *Powder Technol* 58:63–70
27. Bedenko DV, Kovalev OB, Sergachev DV (2022) Numerical study of the gas-particle flows with the two-way coupling formed by coaxial nozzles for laser cladding. *Surf Coat Technol* 445:128700
28. Adnan M, Sun J, Ahmad N, Wei JJ (2021) Comparative CFD modeling of a bubbling bed using a Eulerian–Eulerian two-fluid model (TFM) and a Eulerian-Lagrangian dense discrete phase model (DDPM). *Powder Technol* 383:418–442
29. Li L, Huang Y, Zou C, Tao W (2021) Numerical study on powder stream characteristics of coaxial laser metal deposition nozzle. *Crystals* 11:282
30. Yang SR, Bai HQ, Li CF, Zhang XH, Jia ZQ (2023) Numerical simulation and regression orthogonal experiment optimization of laser cladding of nickel-based superalloy. *Laser Optoelectron Prog* 60:051408
31. Jiang X, Liu A, Yang G, Liu W, Bian H, Suo Y (2022) Low-carbon modeling and process parameter optimization in laser additive manufacturing process. *Aust J Mech Eng* 58:223–238

Publisher's note Springer Nature remains neutral with regard to jurisdictional claims in published maps and institutional affiliations.

Springer Nature or its licensor (e.g. a society or other partner) holds exclusive rights to this article under a publishing agreement with the author(s) or other rightsholder(s); author self-archiving of the accepted manuscript version of this article is solely governed by the terms of such publishing agreement and applicable law.